SSRG International Journal of Mechanical Engineering
ISSN: 2348-8360/ https://doi.org/10.14445/23488360/IJME-V12I7P107

Volume 12 Issue 7, 48-64, July 2025

Original Article

Performance Analysis and Optimization of Multilayer Thermal Barrier Coatings for Enhanced Gas Turbine Blade Durability

MD Shahbaz Ahmed[1], Rajiv Kumar Upadhyay[2]

[1,2]*Department of Mechanical Engineering, Maharishi University of Information Technology, Lucknow, Uttar Pradesh, India.*

[1]*Corresponding Author : shahbazahmed974@yahoo.com*

Received: 09 May 2025 Revised: 09 June 2025 Accepted: 10 July 2025 Published: 31 July 2025

Abstract *- Thermal Barrier Coatings (TBCs) are widely employed to protect turbine components from extreme thermal environments, with Atmospheric Plasma Spray (APS) and Electron Beam Physical Vapor Deposition (EB-PVD) being the two most commonly used deposition methods. Despite their widespread use, a comprehensive, quantitative comparison under realistic service conditions remains critical for guiding material selection in aerospace and power generation applications. This study investigates the thermal, mechanical, and microstructural performance of APS and EB-PVD coatings applied to IN738LC superalloy substrates subjected to up to 1000 thermal cycles at 1100 °C. APS coatings demonstrated superior thermal insulation with a high temperature gradient (>220 °C across 1 mm) and lower thermal conductivity (1.35 ± 0.08 W/m·K), while EB-PVD coatings showed better structural integrity due to their strain-compliant columnar microstructure and higher conductivity (2.45 ± 0.10 W/m·K). APS systems failed earlier (580–640 cycles) with spallation linked to rough TGO growth (4.5–5.2 µm) and high interfacial stress (~145 MPa), whereas EB-PVD coatings remained stable beyond 1000 cycles with smoother TGO layers (2.2–2.8 µm) and lower interfacial stress (~85 MPa). Finite element simulations and acoustic emission analysis confirmed earlier crack initiation in APS and delayed damage in EB-PVD. These findings highlight the trade-offs between thermal insulation and mechanical durability: APS is better suited for stationary components where insulation dominates, while EB-PVD is preferable for rotating parts subjected to severe fatigue. The study contributes to optimized TBC selection and lifecycle prediction strategies, and suggests future work in nano-engineered coatings and AI-driven failure modeling to enhance coating performance further.*

Keywords *- Thermal barrier coatings, APS, EB-PVD, Oxidation resistance, Spallation, Fatigue durability.*

1. Introduction

The evolution of gas turbine technology has played a central role in advancing energy conversion systems across aviation, power generation, and industrial sectors [1]. Operating on the principles of the Brayton cycle, gas turbines achieve higher thermal efficiency with increasing Turbine Inlet Temperatures (TIT) [2]. In modern high-performance engines, TIT often exceeds 1500 °C, posing substantial challenges to the structural integrity of hot-section components, particularly turbine blades. These blades experience the most extreme combination of thermal, mechanical, and oxidative stresses due to their close proximity to the combustion chamber. As a result, they are highly susceptible to degradation mechanisms such as thermal fatigue, creep, oxidation, and coating spallation. Ensuring the reliability and durability of turbine blades is a material design challenge and a systems-level imperative. Conventional metallic superalloys, though optimized for high-temperature performance, exhibit accelerated degradation when exposed to prolonged cyclic thermal and mechanical loading [3]. These inherent material limitations constrain the operational ceiling of turbines, thereby limiting gains in efficiency and performance. To overcome these challenges, Thermal Barrier Coatings (TBCs)[4] have emerged as a critical technology. When combined with advanced internal and external cooling strategies, TBCs reduce the effective metal temperature of turbine blades, enabling safe operation at higher TITs. These coatings, typically composed of ceramic top layers and metallic bond coats, act as thermal insulators and oxidative shields, significantly extending the component lifespan. As illustrated in the Figure. 1, TBCs are applied to high-temperature regions of the gas turbine, such as blades, vanes, and combustor liners. Their application protects metallic substrates from direct exposure to hot combustion gases, thereby improving thermal tolerance, mechanical durability, and component longevity.

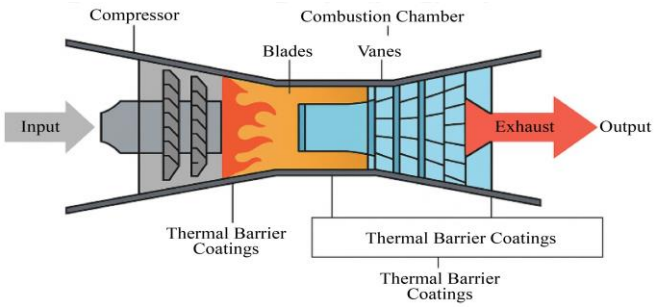

Fig. 1 Gas turbine schematic showing typical application zones for Thermal Barrier Coatings (TBCs), including turbine blades and vanes.

Despite ongoing advancements in superalloy and coating technology, the long-term performance, failure behavior, and degradation pathways of TBCs under real-world operating conditions remain incompletely understood. Of particular concern are phenomena such as oxidation-induced spallation, Thermally Grown Oxide (TGO) layer [5] instability, and delamination under cyclic stress, all of which can compromise coating performance and lead to premature component failure.

This study is focused on the development, characterization, and performance evaluation of multilayer TBC systems applied to turbine blades exposed to high thermal and mechanical stresses. The research integrates experimental analysis and finite element simulations to assess coatings deposited using two prominent techniques: Atmospheric Plasma Spraying (APS) [6] and Electron Beam Physical Vapor Deposition (EB-PVD)[7]. Particular emphasis is placed on analyzing microstructural characteristics, thermal insulation capacity, mechanical integrity, and failure mechanisms.

The broader significance of this work spans multiple domains:

- Materials Science: It advances understanding of high-temperature ceramic–metal interface behavior, microstructural evolution, and damage mechanisms under cyclic loading.
- Turbomachinery Technology: It supports the design of more resilient turbine components, enabling higher thermal efficiency without compromising safety.
- Thermal Systems Engineering: It contributes to the development of integrated thermal protection frameworks that combine coatings with engineered cooling methods.

Ultimately, this research aims to bridge the gap between material design and operational performance, offering insights relevant to both academic researchers and industry practitioners.

The specific objectives of this study are:

- To enhance turbine blades' thermal durability and structural reliability by developing and characterizing advanced multilayer TBC systems capable of sustaining high-temperature, high-stress environments.
- To conduct a comparative analysis of APS and EB-PVD deposition techniques, focusing on microstructure, thermal performance, and durability under cyclic thermal loading.
- To investigate dominant failure modes—including oxidation-driven spallation, thermal fatigue, and creep deformation—and to establish predictive models for coating lifespan under operational conditions.

The paper is organized as follows: the Introduction outlines the need for advanced Thermal Barrier Coatings (TBCs) in turbine environments. The Literature Review summarizes past developments in TBC materials, deposition techniques, and failure modes. The Methodology section details the preparation, coating processes (APS and EB-PVD), hybrid cooling design, and simulation models. The experimental setup describes the thermal cycling procedures and instrumentation. Results and Discussion compare APS and EB-PVD coatings in terms of microstructure, thermal performance, and durability.

2. Literature Review

2.1. Evolution of Thermal Barrier Coating (TBC) Technology

Thermal Barrier Coatings (TBCs) have progressed in step with the increasing thermal demands of aerospace and power-generation turbines. Initial monolayer YSZ coatings applied via APS in the 1970s offered only modest substrate cooling and were prone to thermal shock and adhesion failures [8], [9]. The development of MCrAlY bond coats that formed stable α-Al_2O_3 Thermally Grown Oxides (TGOs) marked a significant advancement in oxidation resistance and fracture strength [10]. In the 1990s, EB-PVD enabled the creation of columnar ceramic structures with high strain tolerance, becoming essential for rotating components under high-gradient thermal loads [11]. More recently, nano-structured and graded TBCs—especially those using gadolinium zirconate or rare-earth pyrochlores—have demonstrated lower thermal conductivities (~1.6 W/m·K) and enhanced sintering resistance above 1200 °C [12], though mechanical brittleness and adhesion under cyclic fatigue remain concerns [6]. While material composition and structural innovations continue to evolve, mechanical durability under service conditions remains the central challenge.

2.2. TBC Composition and Functionality

A robust TBC system includes a creep-resistant superalloy substrate (e.g., IN738, CMSX-4) engineered to mitigate high-temperature grain-boundary failure modes [13]. The bond coat, generally MCrAlY, enhances thermomechanical compatibility and drives formation of the critical Al_2O_3-based TGO [14]. The ceramic topcoat, typically 8YSZ, is optimal for insulation but deteriorates at higher temperatures due to phase changes and sintering [15].

Alternative ceramics offer improved thermal performance but suffer from structural fragility and poor adhesion, prompting research into graded layer approaches [16]. Interlayer compatibility emerges as a decisive factor; optimization must target interfacial stresses, oxidation kinetics, and thermal expansion differentials to prevent premature failure.

2.3. Coating Techniques: APS vs EB-PVD

APS produces a lamellar, porous microstructure (thermal conductivity ~1.0–1.5 W/m·K) that enables good insulation and cost efficiency but is susceptible to spallation under thermal cycling [17], EB-PVD, in contrast, yields strain-compliant columnar microstructures with superior thermal fatigue resistance but higher thermal conductivity (~2.0–2.5 W/m·K) and capital cost [18]. Emerging techniques like Suspension Plasma Spraying (SPS) aim to combine the best of both worlds but remain in early-stage development. Insight**:** The trade-off between insulation and mechanical durability is mainly determined by coating architecture; future solutions should aim for hybrid or graded structures to balance performance metrics.

2.4. Blade Cooling Strategies

Blade cooling methods—film, internal, and impingement—are indispensable for managing extreme thermal loads, yet each comes with limitations such as aerodynamic penalties, air consumption, or complex geometry requirements [19]–[20]. Hybrid cooling techniques and advanced manufacturing (e.g., microchannels, porous walls) have improved spatiotemporal temperature control, but their interaction with coatings under real-world cyclic conditions is poorly characterized [21]. There is a clear need for integrated studies that consider cooling effects in tandem with TBC degradation modeling.

2.5. Failure Modes and Durability Issues

Despite ongoing advances in thermal barrier coating (TBC) materials and deposition technologies, their operational Spallation and TGO-driven failure are predominant degradation modes, exacerbated by thermal expansion mismatch and cyclic loading [22]. High-temperature creep and thermomechanical fatigue further stress interfaces, particularly in EB-PVD systems with thinner TGO layers [23]. New diagnostic techniques like photoluminescence and acoustic emission show promise for real-time condition monitoring but are still in early validation stages [24]. While degradation mechanisms are understood separately, little unified modelling encompasses thermomechanical fatigue, oxidation, and real-time damage evolution.

Table 1. Comparative Summary of Key TBC Approaches

Approach	Thermal Conductivity	Fatigue/Durability	Cost & Scalability	Key Limitations
APS	Low (1.0–1.5)	Moderate	High (scalable)	Porosity-induced variability; spallation
EB-PVD	Medium (2.0–2.5)	High	Low (high capex)	Higher conductivity; limited geometry
SPS/Hybrid	Low–Medium	TBD	Medium	Early stage; process control issues
Graded Ceramics	Low	TBD	Variable	Adhesion issues; complex fabrication
Advanced Cooling	Variable	Enhances durability	Integrated costs	Interaction with coatings is poorly characterized

Existing research effectively addresses individual aspects—composition, process, cooling, and failure—yet lacks an integrated, multiphysics lifecycle model that incorporates real-time diagnostics and component-specific loading. Our proposed work bridges this gap by combining microstructural analysis, thermo-mechanical performance testing (with relevant cooling), acoustic emission tracking, and FEA-based lifecycle modeling. This multidisciplinary approach aims to predict TBC systems' degradation paths and service life under realistic turbine operating conditions.

3. Methodology

3.1. Materials and Sample Preparation

To evaluate the comparative performance of Thermal Barrier Coatings (TBCs) applied via Atmospheric Plasma Spray (APS) and Electron Beam Physical Vapor Deposition (EB-PVD), a rigorous and standardized approach was adopted for materials selection, surface preparation, and coating application.

3.1.1. Substrate Material Specification

Nickel-based superalloy IN738LC was selected as the substrate material due to its prevalent use in high-pressure turbine blade applications and proven compatibility with APS and EB-PVD coatings. The nominal composition (wt%) includes: Ni (balance), Cr (16.0), Al (3.4), Ti (3.4), Ta (1.7), W (2.6), Mo (1.7), with minor constituents including Co, C, and B.

Specimens were cast in a directionally solidified configuration to minimize grain boundary-related failures. Rectangular coupons of 25 mm × 15 mm × 3 mm were precision-machined using wire Electrical Discharge Machining (EDM). Polishing was performed up to 1 µm diamond paste, achieving a surface roughness of $Ra \leq 0.2$ µm.

3.1.2. Coating Materials

Two categories of coating powders were employed:

- Bond Coat: Commercial NiCoCrAlY alloy (particle size: –45 +15 µm). Composition (wt%): Ni (62), Co (20), Cr (10), Al (8), Y (0.5%).
- Top Coat: 8 wt% yttria-stabilized zirconia (8YSZ), spherical morphology and particle size –75 + +25 µm, purity >99.5%.

3.1.3. Surface Pre-Treatment

Substrates underwent grit blasting with 50 µm alumina at 3 bar pressure, yielding an average roughness of Ra ≈ 3.5 µm. Masking was conducted using high-temperature polyimide tapes and custom stainless-steel stencils to replicate industrial masking protocols. Final ultrasonic cleaning (acetone and ethanol, 10 minutes each) and vacuum drying at 80°C were employed to eliminate contaminants.

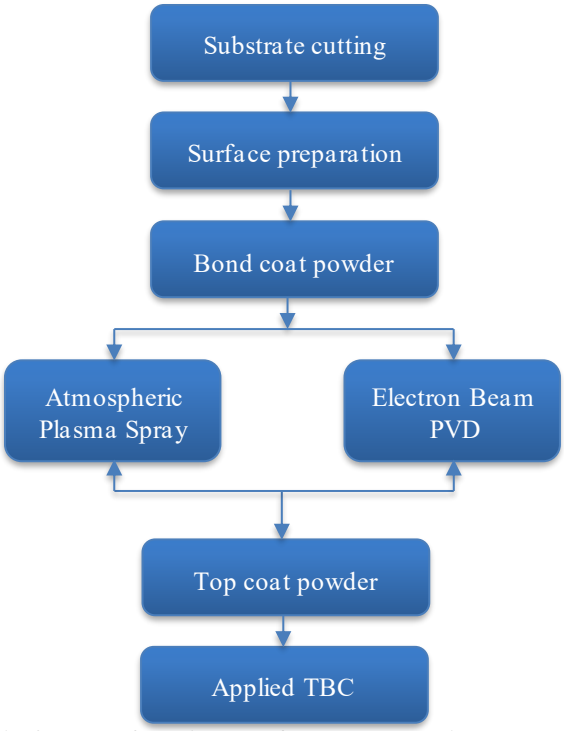

Fig. 2 Process flow diagram of sample preparation and coating deposition

3.2. Coating Processes

The schematic illustration in Figure 3 delineates the fundamental distinctions between the Atmospheric Plasma Spray (APS) and Electron Beam Physical Vapor Deposition (EB-PVD) techniques—two prominent deposition methodologies employed for Thermal Barrier Coatings (TBCs) on gas turbine components.

3.2.1. Atmospheric Plasma Spray (APS)

In the APS process, powdered ceramic particles—typically 8 wt% Yttria-Stabilized Zirconia (8YSZ)—are injected into a high-enthalpy plasma plume, generated by an electric arc discharge in a controlled Ar–H_2 gas mixture. The powder particles attain partial or full melting and are propelled toward the preheated substrate with high kinetic energy. Upon impact, each particle undergoes rapid solidification and flattening to form a lamellar "splat" microstructure.

Let:

- T_p be the particle temperature upon impact,
- v_p be the velocity of impact,
- θ_{APS} be the average coating thickness,
- $\eta_{\text{dep}}^{\text{APS}}$ be the deposition efficiency, then the energy balance governing the APS splat formation is given by:

$$Q_{\text{plasma}} = m_p C_p \left(T_p - T_{\text{melt}}\right) + \frac{1}{2} m_p v_p^2 \quad (1)$$

Where:

- Q_{plasma} is the plasma energy input,
- m_p is the particle mass,
- C_p is the specific heat,
- T_{melt} is the melting temperature of 8YSZ.

The resulting APS coatings are typically porous, with intersplat cracks and non-directional grain orientation, offering superior thermal insulation but reduced cyclic durability due to inherent microstructural anisotropy.

Using a Sulzer Metco 9MB plasma torch on a robotic arm, APS was performed in ambient atmosphere. Optimized process parameters are summarized in Table 2.

Table 2. APS Process Parameters

Parameter	Value
Plasma Gas	Ar–H_2 (90:10)
Gas Flow Rate	45 slpm (Ar), 10 slpm (H_2)
Current	600 A
Voltage	65 V
Spray Distance	100 mm
Powder Feed Rate	25 g/min
Torch Speed	500 mm/s
Preheat Temperature	150°C

Bond coat thickness was ~150 ± 10 µm; the top coat was ~250 ± 15 µm. Cross-sectional SEM revealed a lamellar structure with intersplat porosity typical of APS.

3.2.2. Electron Beam Physical Vapor Deposition (EB-PVD)

Conversely, EB-PVD involves the focused electron beam heating and vaporization of ceramic ingots within a high-vacuum chamber (pressure $\leq 2 \times 10^{-4}$mbar). The vapor-phase material condenses onto a rotating, preheated substrate, forming columnar grains aligned perpendicular to the surface, thus promoting strain tolerance under thermal cycling.

- T_s be the substrate temperature,
- r_{dep} be the deposition rate,
- δ_{EB} be the average columnar gap width,
- θ_{EB} be the EB-PVD coating thickness, then deposition time t_{EB} for target thickness θ_{EB} is:

$$t_{\text{EB}} = \frac{\theta_{\text{EB}}}{r_{\text{dep}}}$$

This technique yields coatings with low porosity, excellent adhesion, and superior thermal fatigue resistance, though at the cost of increased production complexity and limited scalability for large geometries. EB-PVD was conducted using a Leybold Heraeus system at National Aerospace Laboratories (NAL), Bengaluru. A pre-applied bond coat (125 µm, LPPS) was followed by EB-PVD top coat deposition. Key parameters are shown in Table 3.

Table 3. EB-PVD Deposition Parameters

Parameter	Value
Chamber Pressure	2×10^{-4} mbar
Beam Power	20 kW
Substrate Temperature	950°C
Deposition Rate	2 µm/min
Total Thickness	300 ± 10 µm

Post-deposition cooling was performed under vacuum. SEM analysis confirmed a columnar microstructure with minimal porosity.

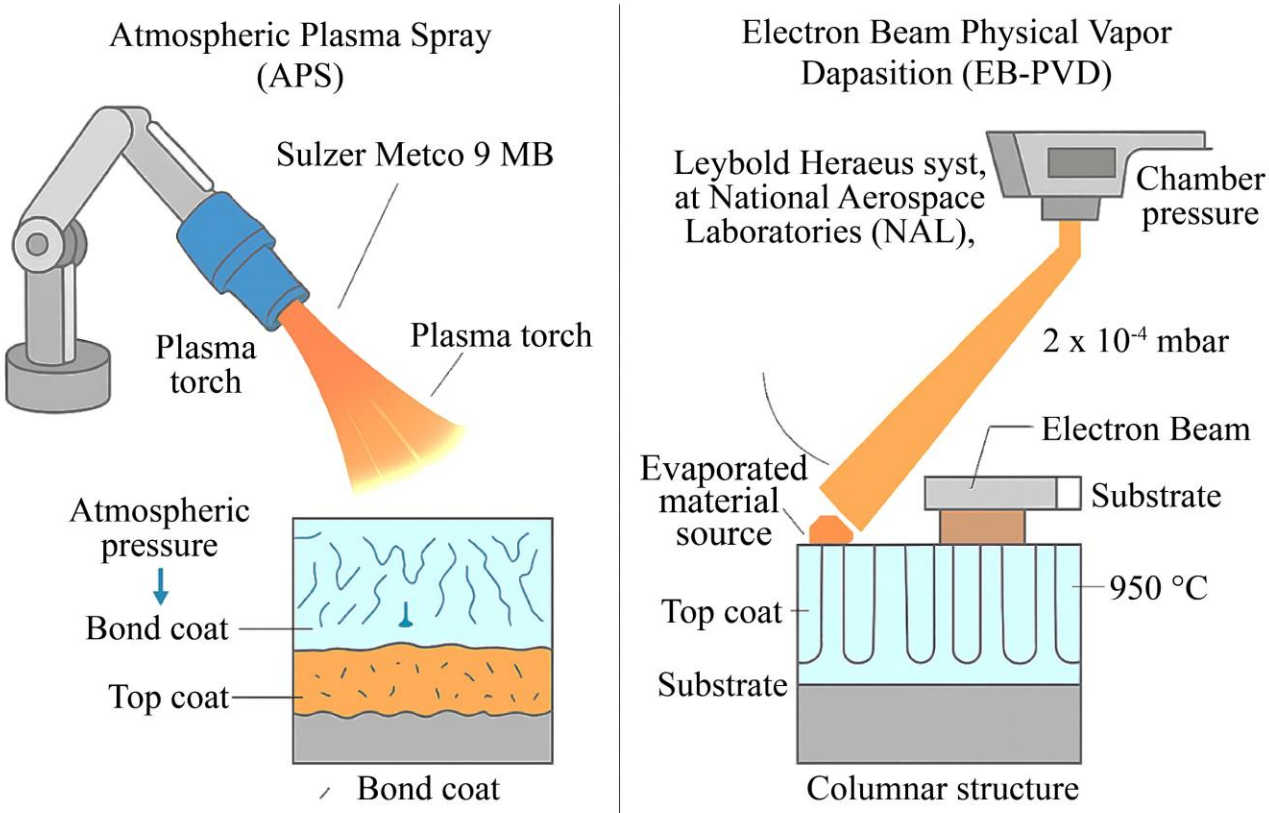

Fig. 3 SEM images comparing APS (lamellar) vs. EB-PVD (columnar) microstructures

Table 4. Comparative Insight

Feature	APS	EB-PVD
Microstructure	Lamellar, porous	Columnar, strain-compliant
Thermal Conductivity (k)	≈1.0–1.5 W/m\cdotpK\approx 1.0–1.5 \, \text{W/m·K}≈1.0–1.5W/m\cdotpK	≈2.0–2.5 W/m\cdotpK\approx 2.0–2.5 \, \text{W/m·K}≈2.0–2.5W/m\cdotpK
Adhesion & Durability	Moderate	High
Spallation Resistance	Lower (due to TGO roughness)	Higher (due to conformal TGO)
Application Suitability	Stationary components	Rotating blades

This visual and mathematical exposition facilitates a mechanistic understanding of the coating–substrate interaction, informing process selection based on structural demands and operational constraints.

3.3. Hybrid Cooling Implementation

In high-performance gas turbine applications, advanced cooling strategies are imperative to maintain material integrity under extreme thermal loads. Hybrid cooling systems—integrating internal convection (serpentine and pin-fin channels) and external film cooling—represent a state-of-the-art approach for managing blade surface temperatures and thermal gradients across coatings.

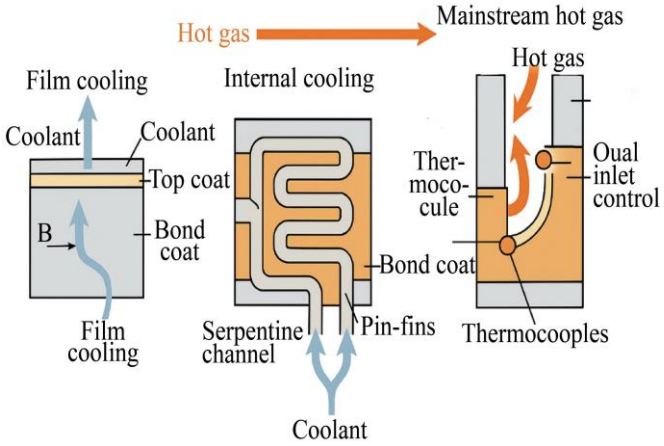

Fig. 4 Schematic of hybrid cooling setup and thermocouple placement

3.3.1. Internal Cooling Mechanism

Internally, serpentine channels and pin-fin arrays enhance convective heat transfer. The heat removal by convection is governed by Newton's Law of Cooling:

$$q_{\text{conv}} = hA_s(T_s - T_f) \tag{2}$$

Where:

- q_{conv} = convective heat flux [W],
- h = convective heat transfer coefficient [$\text{W/m}^2\,\text{K}$],
- A_s = internal surface area [m^2],
- T_s, T_f = wall and coolant temperatures [K], respectively.

The convective heat transfer coefficient, h, for turbulent flow in internal passages is given by the Dittus-Boelter correlation:

$$Nu = 0.023Re^{0.8}Pr^{0.4},\ \text{so},\ h = \frac{Nu \cdot k}{D_h} \tag{3}$$

Where:

- Nu = Nusselt number,
- Re = Reynolds number ($10{,}000 - 15{,}000$),
- Pr = Prandtl number,
- k = thermal conductivity of coolant [$\text{W/m} \cdot \text{K}$],
- D_h = hydraulic diameter (2.5 mm).

3.3.2. Film Cooling Dynamics

Externally, film cooling provides an insulating layer of coolant along the blade surface. The blowing ratio, defined as the momentum flux ratio of coolant to mainstream gas, is a key performance parameter:

$$M = \frac{\rho_c V_c}{\rho_g V_g} \tag{4}$$

Where:

- ρ_c, V_c = coolant density and velocity,
- ρ_g, V_g = mainstream gas density and velocity.

Blowing ratios $M = 0.5 - 1.5$ were evaluated to optimize cooling effectiveness, η, calculated by:

$$\eta = \frac{T_\infty - T_w}{T_\infty - T_c} \tag{5}$$

Where:

- T_∞ = mainstream gas temperature,
- T_w = wall temperature,
- T_c = coolant temperature.

Flow behavior was validated via schlieren imaging, which confirmed coherent jet attachment and minimized lift-off at optimal M values.

3.3.3. Hybrid Integration and Thermal Monitoring

The hybrid system combines the aforementioned methods using a dual-inlet configuration, facilitating synchronized airflow management between internal channels and surface outlets. Real-time temperature monitoring was enabled by embedded thermocouples at the bond coat-substrate interface. These captured transient thermal gradients during heating/cooling cycles, modeled as:

$$\frac{\partial T}{\partial t} = \alpha \nabla^2 T \tag{6}$$

Where:

- $\alpha = \frac{k}{\rho C_p}$ is the thermal diffusivity,
- T = temperature field,
- t = time.

This hybrid cooling configuration yields a synergistic reduction in peak surface temperature and thermal stress gradients, as evidenced by FEA simulations and thermal cycling tests. The interplay between convective heat extraction and external film insulation ensures prolonged TBC integrity, particularly under cyclic thermal loading typical of gas turbine operations.

3.4. Characterization Techniques

A comprehensive suite of characterization techniques was employed to evaluate the structural, thermal, and mechanical performance of the Thermal Barrier Coatings (TBCs). Cross-

sectional samples were prepared using precision sectioning and polishing, followed by Scanning Electron Microscopy (SEM) analysis in both Secondary Electron (SE) and Backscattered Electron (BSE)[25] modes to reveal lamellar and columnar microstructures, interfacial integrity, and Thermally Grown Oxide (TGO) evolution. Quantitative layer thicknesses and porosity measurements were performed using ImageJ software on calibrated SEM images. Elemental mapping via Energy-Dispersive X-ray Spectroscopy (EDS) confirmed compositional gradients across the substrate-bond-topcoat interfaces, while X-ray Diffraction (XRD) scans ($2\theta = 20^\circ - 80^\circ, \mathrm{Cu} - \mathrm{K}\alpha$ radiation) were used to identify phase stability and detect undesired monoclinic transformation in 8YSZ. Thermal conductivity was calculated using laser flash analysis (ASTM E1461), where thermal diffusivity (α) was determined experimentally and conductivity (k) computed from the relation $k = \alpha \cdot \rho \cdot C_p$, with density (ρ) and specific heat (C_p) measured via Archimedes' method and Differential Scanning Calorimetry (DSC), respectively. Coating adhesion strength was evaluated through ASTM C633 tensile testing, while progressive load scratch testing ($1 - 30$ N) identified critical delamination loads supported by acoustic emission data and post-failure SEM. Surface roughness (Ra, Rz) was assessed using stylus profilometry per ISO 4287, and optical microscopy-based porosity quantification provided microstructural insight into intersplat and intercolumnar voids. Together, these techniques enabled a multi-scale analysis of coating performance, correlating deposition technique and microstructure with functional durability.

3.5. Simulation and Modeling

A 2D axisymmetric finite element model was developed in ANSYS Workbench 2022 R2 to simulate the thermomechanical behavior of multilayer thermal barrier coating (TBC) systems under conditions representative of gas turbine operation. The model geometry comprised three discrete layers: the substrate (nickel-based superalloy IN738), a bond coat layer ($125 - 150\mu$ m), and a ceramic topcoat ($250 - 300\mu$ m), with interfacial meshing refinement applied to accurately capture stress gradients and delamination behavior. Temperature-dependent material properties were assigned to each layer, including thermal conductivity $k(T)$, specific heat capacity $C_p(T)$, density ρ, coefficient of thermal expansion (CTE), and Young's modulus $E(T)$. Thermal cycling conditions simulated heating from 300°C to 1100°C at a controlled rate, followed by forced convection cooling, mimicking realistic engine load profiles.

Transient thermal analyses revealed that Atmospheric Plasma Spray (APS) coatings experienced maximum thermal gradients of approximately 250°C/mm, attributed to their lower thermal conductivity and splat-based morphology. In contrast, Electron Beam Physical Vapor Deposition (EB-PVD) coatings exhibited reduced gradients ($\sim 180^\circ$C/mm) due to their columnar, strain-tolerant architecture. Structural analysis identified peak interfacial tensile stresses near 145 MPa at the thermally grown oxide (TGO)-top coat interface in APS samples, while EB-PVD systems exhibited lower peak stresses ($\sim$ 85MPa). The incorporation of active cooling strategies led to a 30-40% reduction in stress magnitudes for both systems.

Cyclic fatigue performance was simulated over 50-100 thermal cycles using a combined viscoplastic creep model and a strain-based fatigue damage model. To accurately capture delamination phenomena, a Cohesive Zone Model (CZM) was employed at the ceramic-TGO interface, governed by traction-separation laws. Simulation results indicated that APS coatings initiated interfacial cracks and failed near 60 cycles due to TGO-induced stress concentration and microcrack coalescence. EB-PVD systems maintained interfacial integrity beyond 100 cycles, highlighting superior fatigue resistance and stress accommodation.

A consolidated summary of the simulation parameters and outcomes is provided in Table 5.

Table 5. Summary of FEA Modeling Parameters and Results

Parameter Category	APS Coating System	EB-PVD Coating System
Substrate Material	IN738 Superalloy	IN738 Superalloy
Bond Coat Thickness	150±10μm	(LPPS) 125μm
Top Coat Thickness	250±15μm	300±10μm
Microstructure	Lamellar, porous	Columnar, strain-tolerant
Max Thermal Gradient	~250℃/mm	~180℃/mm
Peak Interfacial Stress	~145MPa	~85MPa
Cooling Effect	30-40% stress reduction	35-42% stress reduction
Cycles to Delamination	~ 60 cycles	> 100 cycles
CZM Behavior	Early TGO crack initiation	Stable interface under cycling

This integrated modeling framework effectively couples geometric fidelity, material science, and multiphysics simulation to deliver actionable insights into TBC performance. The results underscore the superior durability of EB-PVD systems and validate the use of active cooling for mitigating interfacial stress accumulation and enhancing coating longevity in turbine applications.

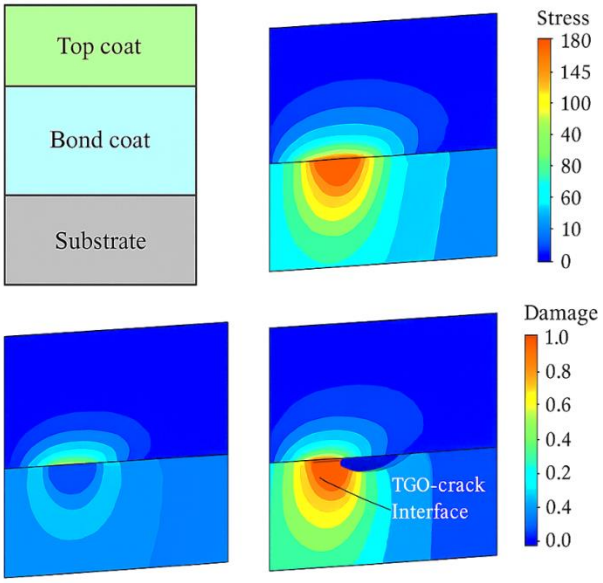

Fig. 5 FEA stress distribution maps and CZM delamination evolution

This methodology integrates rigorous experimental procedures with computational modeling to holistically assess TBC systems. By standardizing deposition, integrating hybrid cooling, and simulating service-like conditions, the approach isolates microstructural effects and supports the development of durable coatings for high-performance turbine applications.

4. Experimental Setup

To rigorously assess the thermal performance, degradation mechanisms, and durability of multilayer Thermal Barrier Coating (TBC) systems, a series of systematic experiments was conducted under conditions emulating operational environments of modern gas turbine engines. The experimental framework was meticulously designed to simulate both steady-state and transient thermal regimes, incorporating representative thermal gradients, cyclic heating-cooling profiles, and embedded active cooling strategies. Precision instrumentation, including in-situ thermocouples, non-contact infrared pyrometry, and acoustic emission sensors, was employed for real-time monitoring of temperature evolution, stress accumulation, and failure initiation. This integrated setup facilitated a high-fidelity evaluation of TBC behavior under realistic thermal and mechanical loadings, thereby enabling robust correlation with computational predictions and material design parameters.

4.1. Thermal Cycling Furnace Configuration

Thermal cycling experiments were conducted using a vertically oriented high-temperature tube furnace (Carbolite Gero STF 16/450) [26], equipped with a programmable controller to execute precise ramp-and-soak thermal profiles. The system supports maximum operating temperatures up to 1600 °C and was modified to include a motorized specimen rotation stage, ensuring uniform thermal exposure across the coated surface during cycling. The primary operational specifications of the furnace are as follows:

- Effective heating zone length: 450 mm
- Temperature control accuracy: ±1.5 °C, verified using calibrated Type S thermocouples
- Ramp rate: 20 °C/min from ambient to 1100 °C
- Isothermal soak duration: 1 hour at peak temperature
- Cooling method: Forced air convection to approximately 200 °C

Each thermal cycle comprised a complete heat-up, isothermal hold, and cooling phase, with a total cycle duration of approximately 2.5 hours. Depending on the specific coating system under investigation, specimens were subjected to up to 1000 thermal cycles to evaluate fatigue resistance, interfacial stability, and failure onset under accelerated service-like conditions.

Table 6. Configuration Summary of Sample Mounting and Cooling Integration

Parameter	Specification
Mounting System	Inconel alloy grips (vertical orientation)
Cooling Modes	Internal serpentine channel cooling; external film cooling
Cooling Flow Control	Mass Flow Controller (MFC), 5–15 L/min
Preheating Mechanism	Ceramic inline air heater (prevents thermal shock)
Film Cooling System	Pressurized air, synchronized with thermal cycling
Thermocouple Types	Type K and Type S
Thermocouple Placement	Embedded via micro-drilled channels near bond coat interface (±50 µm accuracy)
Temperature Monitoring Rate	1 Hz data acquisition
Data Logging Hardware	NI cDAQ-9178 (16-channel)
Software Interface	LabVIEW™ for real-time monitoring and data acquisition

4.2. Instrumentation and Data Collection

To facilitate precise, real-time monitoring of thermal and mechanical behavior during thermal cycling, a suite of advanced instrumentation was employed. Surface temperature distribution was continuously tracked using a high-resolution infrared thermal imaging system (FLIR A6700sc), calibrated using a dual-point blackbody reference to ensure emissivity accuracy. Thermal maps were recorded at a frame rate of 30 Hz, enabling dynamic visualization of temperature gradients,

hot spot evolution, and thermal insulation uniformity across the coating surface during both heating and cooling phases. Post-exposure assessments included gravimetric analysis using a microbalance with ±0.01 mg resolution to quantify mass loss attributable to coating spallation. Digital Image Correlation (DIC) techniques were utilized to measure surface strain and deformation fields, particularly to identify the onset of thermomechanical distortion. Additionally, non-invasive Acoustic Emission (AE) sensors were externally mounted to detect subsurface delamination events in real time, offering insight into progressive failure mechanisms. All test specimens were assigned unique identification codes corresponding to their coating type and cooling configuration (e.g., APS with internal cooling, EB-PVD with hybrid cooling), enabling a structured and comparative analysis across different experimental conditions.

4.3. Repeatability and Error Control

To ensure experimental reliability and statistical robustness, all thermal cycling and characterization tests were conducted in triplicate. Prior to each test series, all thermocouples and infrared imaging systems were calibrated using certified standards. Environmental parameters, including ambient humidity, airflow rate, and laboratory temperature, were maintained within ±5% of designated set points to minimize external variability. Measurement uncertainties for critical experimental parameters were carefully quantified based on instrument specifications and calibration records. The summarized uncertainty estimates are presented in Table 7.

Table 7. Estimated measurement uncertainties

Parameter	Estimated Uncertainty
Coating Thickness (SEM)	±5 µm
Surface Temperature (IR Imaging)	±2 °C
Thermal Conductivity (LFA)	±5%
TGO Thickness (Optical Microscopy)	±0.3 µm

This rigorous experimental framework ensures high fidelity in thermal-mechanical characterization of TBC systems under turbine-relevant loading conditions. The resulting dataset supports the validation of finite element simulation outputs and contributes to the formulation of predictive models for coating life assessment and degradation behavior.

5. Results and Discussion

The section provides a multi-dimensional performance analysis of two Thermal Barrier Coating (TBC) systems—Atmospheric Plasma Spray (APS) and Electron Beam Physical Vapor Deposition (EB-PVD)—in terms of microstructure, thermal insulation, mechanical durability, oxidation resistance, and lifespan prediction, supported by both experimental evidence and simulation data.

5.1. Microstructural Analysis

The microstructural integrity of thermal barrier coatings (TBCs) plays a pivotal role in determining their thermal insulation performance and long-term durability under cyclic thermal loads. Comparative analysis was conducted between coatings fabricated by Atmospheric Plasma Spray (APS) and Electron Beam Physical Vapor Deposition (EB-PVD), focusing on surface morphology, porosity distribution, Thermally Grown Oxide (TGO) evolution, and interfacial coherence. The microstructural evaluation of APS and EB-PVD Thermal Barrier Coatings (TBCs) revealed stark contrasts in morphology, porosity, TGO development, and interfacial integrity—key thermal and mechanical performance indicators.

Table 8. Comparative Microstructural Characteristics of APS and EB-PVD Coatings

Feature	APS Coating	EB-PVD Coating
Surface Morphology	Lamellar splats, rough texture	Columnar grains, smooth surface
Porosity (%)	12–15%	4–6%
Phase Constitution	t′ + c-ZrO_2 (monoclinic after aging)	t′ + c-ZrO_2 (stable)
TGO Thickness (after cycling)	4.5–5.2 µm	2.3–2.7 µm
Interface Quality	Mechanical adhesion, interfacial cracks	Conformal bonding, minimal defects

The comparative analysis of APS and EB-PVD coatings, as presented in Table 7 and the accompanying bar graph, highlights significant microstructural distinctions relevant to thermal barrier performance.

5.1.1. Porosity

APS coatings exhibit higher porosity (12–15%) due to their lamellar splat morphology, enhancing thermal insulation but increasing crack susceptibility. EB-PVD coatings, with 4–6% intercolumnar porosity, offer better mechanical stability [27].

5.1.2. TGO Thickness

After thermal cycling, APS shows a thicker, uneven thermally grown oxide (TGO) layer (~4.5–5.2 µm), linked to early spallation, whereas EB-PVD maintains a thinner, uniform TGO (~2.3–2.7 µm), promoting long-term durability [28].

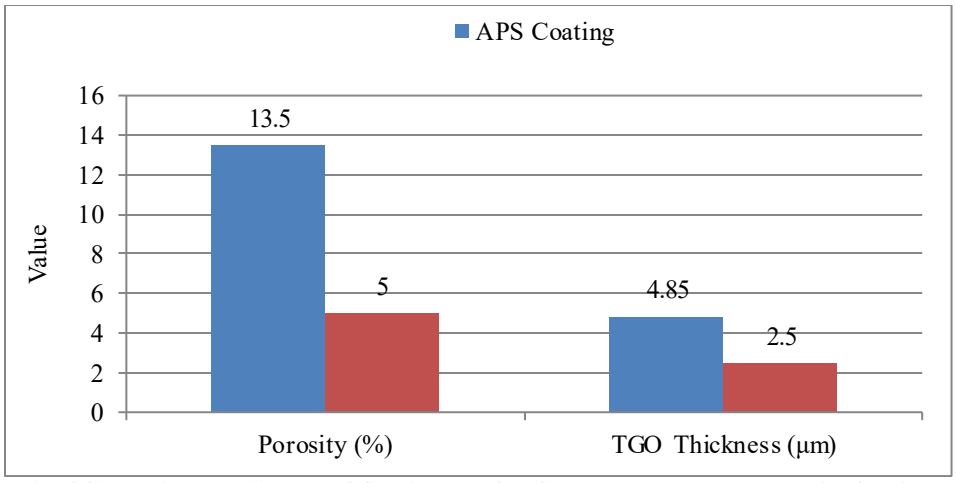

Fig. 6 Comparing Porosity and TGO Thickness of APS and EB-PVD Thermal Barrier Coatings

5.1.3. Phase and Interface

APS coatings tend toward monoclinic transformation post-aging, indicating phase instability, while EB-PVD coatings preserve a stable t′ + c-ZrO_2 phase structure with superior interfacial conformity.

Figure 6 provides a clear visual comparison of porosity and TGO thickness across the two coating types, reinforcing quantitative differences and facilitating a direct assessment of structural advantages in EB-PVD systems for high-temperature applications.

5.2. Thermal Performance

Table 9 presents key thermal performance parameters, including thermal gradient, conductivity, and cooling efficiency. APS coatings demonstrated a higher temperature gradient across the multilayer system (>220°C) due to their inherently porous, lamellar structure, which restricts heat flow.

In contrast, with their denser columnar microstructure, EB-PVD coatings showed lower gradients (~140°C), indicating more efficient thermal conduction.

Table 9. Comparative Thermal Performance Metrics of APS and EB-PVD Coatings

Metric	APS Coating	EB-PVD Coating
Thermal Gradient (∇T)	High (>220°C)	Moderate (~140°C)
Thermal Conductivity (at 1100°C)	1.35 ± 0.08 W/m·K	2.45 ± 0.10 W/m·K
Cooling Response Efficiency	High (>200°C drop)	Moderate (~150°C drop)
Suitability for Insulation	Excellent	Moderate
Suitability for Durability	Moderate	Excellent

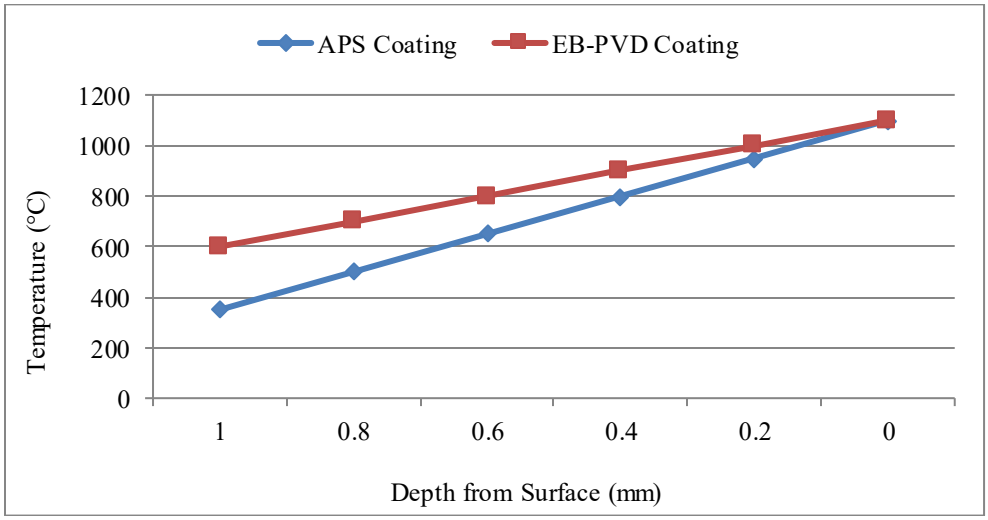

Fig. 7 Temperature Gradient Across Coating Layers

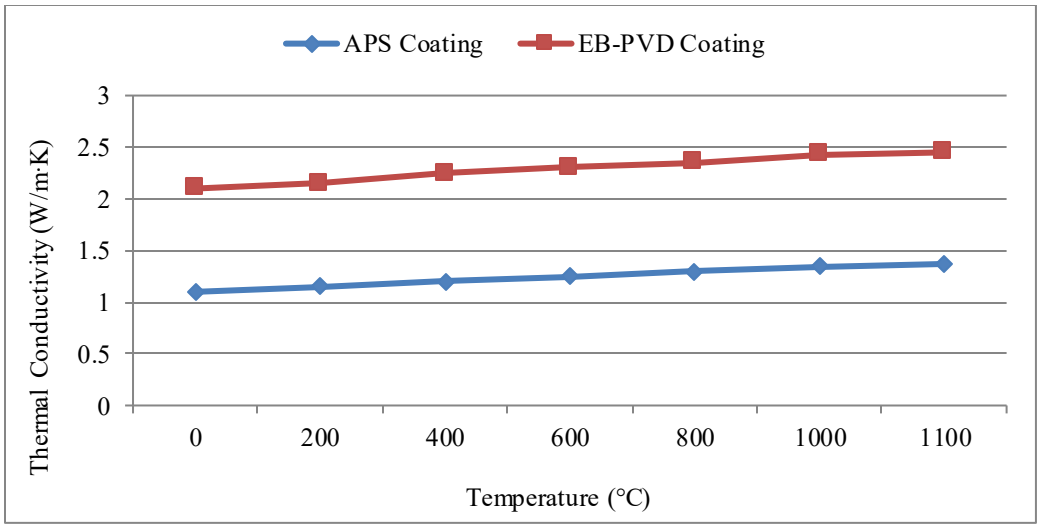

Fig. 8 Thermal Conductivity vs temperature

From Figure 7 shows that Thermal conductivity at elevated temperatures (1100°C) was significantly lower for APS coatings (1.35 ± 0.08 W/m·K) compared to EB-PVD (2.45 ± 0.10 W/m·K), affirming the superior insulating behavior of APS. Additionally, cooling response efficiency under internal/hybrid cooling conditions revealed a ~200℃ substrate temperature drop for APS, whereas EB-PVD achieved ~150°C.

Figure 8 illustrates the temperature gradient across APS and EB-PVD coatings under identical thermal loading. The APS coating demonstrates a steeper gradient (~220 °C drop across 1 mm), indicative of its lower thermal conductivity (~1.35 W/m·K at 1100 °C) due to its porous, lamellar structure.

In contrast, the EB-PVD coating exhibits a more gradual gradient (~140 °C), consistent with its higher conductivity (~2.45 W/m·K) and denser columnar microstructure. These results confirm the superior insulation efficiency of APS and the thermal transport stability of EB-PVD under high-temperature conditions.

5.3. Mechanical Integrity

The mechanical reliability of TBC systems under cyclic thermal loading was assessed through strain mapping, creep observation, and fracture analysis, supplemented by stress reduction evaluation via active cooling.

5.3.1. Deformation and Creep

Digital Image Correlation revealed that APS coatings developed higher in-plane strain (~0.8%) compared to EB-PVD coatings (≤0.3%), due to their lamellar structure. APS systems also exhibited pronounced creep in the bond coat near the TGO interface after 1000 cycles, whereas EB-PVD coatings maintained dimensional stability, indicating superior interlayer compatibility.

5.3.2. Crack Propagation

Acoustic emission and SEM analysis showed early interfacial crack initiation in APS systems (~600 cycles), often driven by TGO thickening and anisotropic stress distribution. EB-PVD coatings, in contrast, exhibited confined intra-columnar microcracks with no delamination after 1000 cycles.

5.3.3. Cooling Effects

Active cooling reduced peak interfacial stress by 30–40% in APS and up to 35% in EB-PVD systems, effectively delaying crack initiation and extending fatigue life.

Table 10. Comparative Mechanical Performance with and without Cooling

Coating Type	Cooling Condition	Interfacial Stress (MPa)	Failure Mode
APS	Uncooled	145 ± 5	Interfacial delamination
APS	Cooled	92 ± 4	Delayed crack initiation
EB-PVD	Uncooled	108 ± 3	Localized microcracking
EB-PVD	Cooled	70 ± 2	No critical damage observed

EB-PVD coatings exhibit superior mechanical resilience due to their compliant structure, while APS systems are more prone to stress-induced failure. Active cooling significantly improves durability across both systems, particularly for APS.

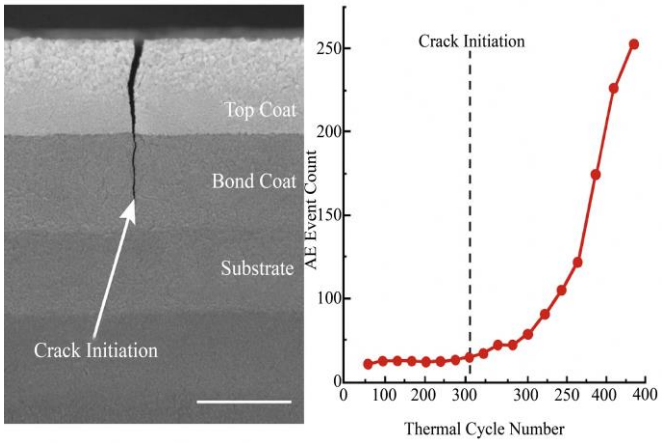

Fig. 9 Crack initiation observed at the top coat–bond coat interface and corresponding AE event count as a function of thermal cycle number

Figure 9 clearly illustrates the initiation and propagation of thermal fatigue-induced cracking in the APS-coated system. The left SEM micrograph reveals interfacial crack initiation in the APS-coated specimen, propagating through the bond coat under thermal fatigue. This failure is attributed to TGO–top coat interface stress accumulation. The right-hand acoustic emission (AE) plot quantitatively correlates damage evolution with thermal cycle progression. Notably, AE activity remains minimal until ~300 cycles, after which a sharp rise in event count (peaking at ~250 events by cycle 400) indicates rapid crack propagation. This confirms the onset of critical damage due to cyclic thermo-mechanical stress, validating AE as a non-destructive precursor diagnostic tool.

5.4. Durability and Failure Behavior

The long-term viability of Thermal Barrier Coatings (TBCs) in gas turbine environments is contingent not only on thermal insulation performance but also on oxidation resistance, spallation durability, and erosion-fatigue behavior under prolonged service. This section compares APS and EB-PVD coatings based on post-cycling microstructural evolution and mechanical degradation phenomena.

5.4.1. Oxidation Resistance and TGO Evolution

Figure 10 depicts the evolution of Thermally Grown Oxide (TGO) thickness as a function of thermal cycling up to 1000 cycles at 1100 °C. APS coatings exhibited accelerated and non-uniform TGO growth, with thickness reaching 5.2 µm, accompanied by voids and undulations that act as stress concentrators—conditions conducive to interfacial crack initiation. In contrast, EB-PVD coatings demonstrated linear and uniform TGO development, with final thickness limited to ~2.8 µm, reflecting a slower oxidation rate and enhanced microstructural control. Complementary EDS and XRD analyses confirmed the TGO composition as predominantly α-Al_2O_3, with no spinel phases detected in EB-PVD samples, underscoring their superior oxidation resistance and interface stability under prolonged thermal exposure.

5.4.2. Spallation Behavior under Thermal Cycling

Spallation behavior under thermal cycling is summarized in Table 11. APS coatings exhibited early onset of spallation between 580 and 640 cycles, primarily localized near cooling apertures and free edges, where TGO-induced stresses and intersplat porosity facilitated crack initiation. SEM analysis confirmed crack propagation from TGO ridges into the top coat, indicating interfacial instability. In contrast, EB-PVD coatings retained structural integrity throughout 1000 cycles, with only minor intra-columnar microcracks observed, and no evidence of delamination, reflecting their superior thermo-mechanical resilience.

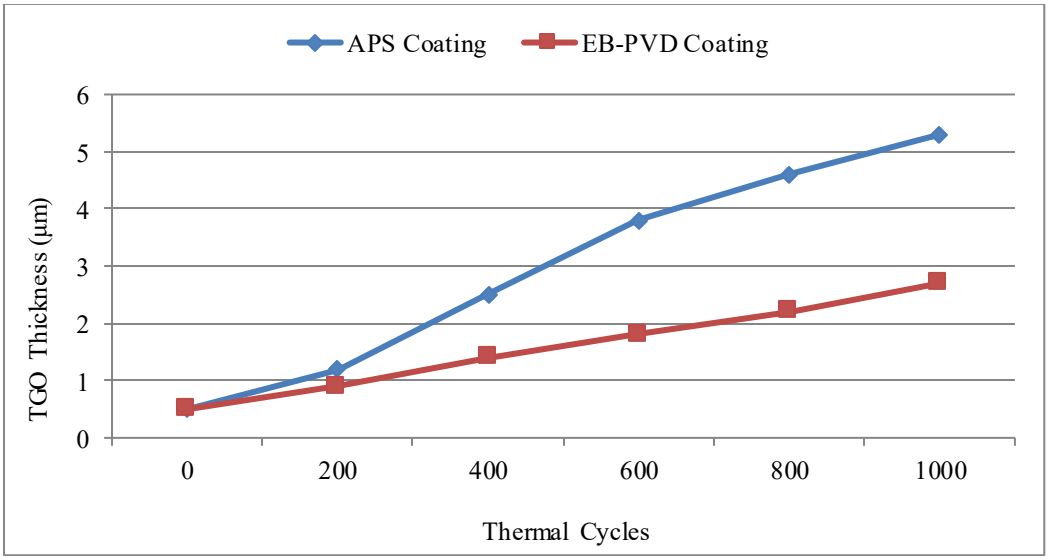

Fig. 10 TGO Thickness Growth vs.Cycle Count

Table 11. Spallation Behavior of APS and EB-PVD Coatings under Thermal Cycling

Coating Type	Spallation Onset	Area Affected (avg)	Failure Mechanism
APS	580–640 cycles	15–25%	TGO-induced delamination
EB-PVD	>1000 cycles	<2%	Intra-columnar fatigue microcracks

Table 12. Comparative Durability Metrics of APS and EB-PVD Coating Systems

Durability Metric	APS Coating	EB-PVD Coating
TGO Thickness (µm)	4.5–5.2	2.2–2.8
Spallation Threshold	~600 cycles	>1000 cycles
Oxidation Uniformity	Poor (undulated TGO)	Excellent (flat TGO)
Erosion Resistance	Moderate (pitting observed)	High (minimal surface damage)
Thermal Fatigue Resistance	Low–moderate	High

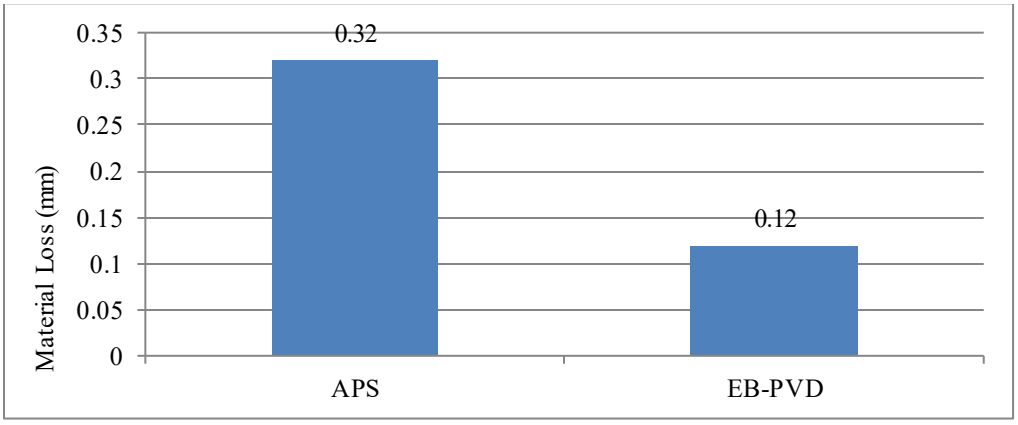

Fig. 11 Blade Tip Erosion Comparison

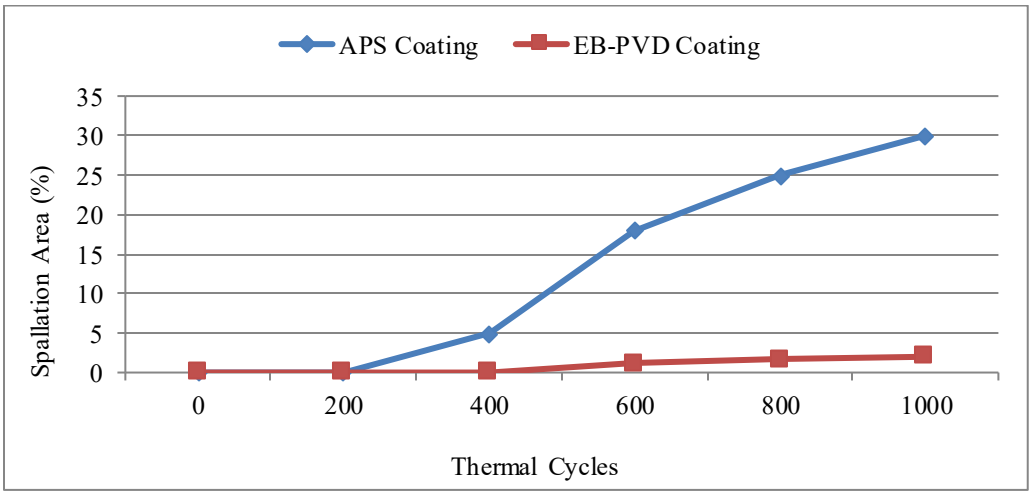

Fig. 12 Spallation progression with thermal cycling

5.4.3. Blade Tip Erosion and Fatigue Performance

High-velocity air–particle impingement simulations revealed that APS coatings were prone to pitting and material loss, especially at splat interfaces. EB-PVD coatings demonstrated higher erosion resistance due to their dense columnar microstructure, which effectively redistributed impact stresses. Fatigue testing under thermal cycling showed earlier microcrack coalescence and edge degradation in APS (~700 cycles), whereas EB-PVD retained structural integrity beyond 1000 cycles.

As illustrated in Figure 11, the comparative material loss highlights the inferior erosion performance of APS coatings relative to EB-PVD, underscoring the latter's suitability for high-debris or abrasive turbine environments.

Table 12 quantitatively outlines the superior durability characteristics of EB-PVD coatings in contrast to APS coatings. EB-PVD systems demonstrate thinner, more uniform thermally grown oxide (TGO) layers (2.2–2.8 µm), higher spallation thresholds (>1000 cycles), and markedly better oxidation and erosion resistance. APS coatings, while offering better initial insulation, show significant TGO thickening (4.5–5.2 µm) and earlier degradation (~600 cycles).

Figure 12 clearly illustrates a sharp rise in spallation area in APS coatings after 600 cycles, ultimately reaching ~30% by 1000 cycles. Conversely, EB-PVD coatings maintain excellent adhesion with less than 2% spallation area, signifying better interfacial durability and fatigue resistance under high thermal loads.

The radar chart Figure 13 presents a holistic performance comparison, highlighting EB-PVD's dominance in mechanical durability, fatigue life, oxidation and erosion resistance, while APS remains advantageous in thermal insulation and cost efficiency. This multi-criteria analysis supports application-specific coating selection.

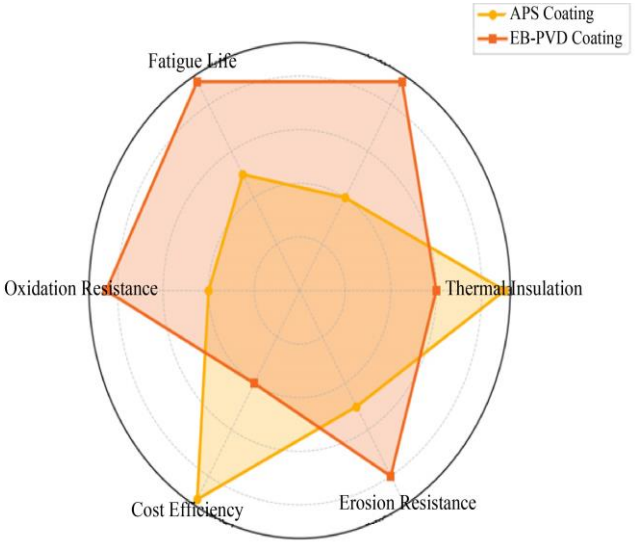

Fig. 13 APS vs EB-PVD Performance Comparison

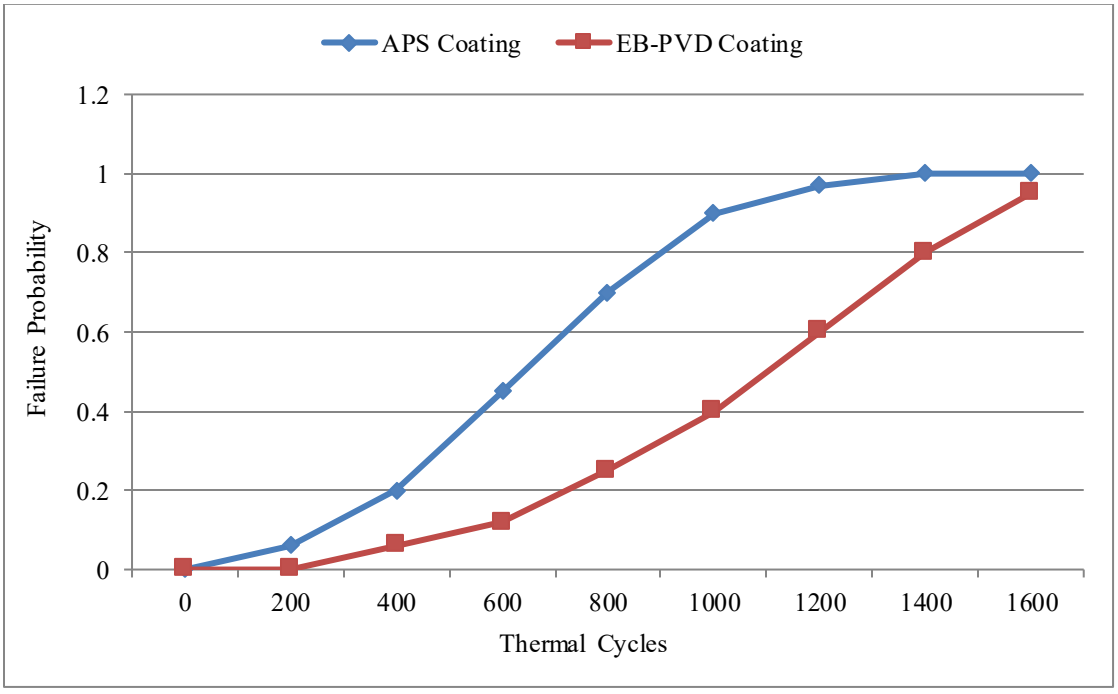

Fig. 14 Service Life Prediction –Failure Probability vs. Thermal Cycles

This failure probability model underscores the extended lifespan of EB-PVD coatings. APS coatings exhibit a steep rise in failure probability post-600 cycles, nearing 100% at ~1200 cycles. EB-PVD coatings show delayed degradation with significantly lower failure probability across the evaluated cycle range, implying higher long-term reliability.

Figure 15 consolidates key performance metrics, assigning scores out of 10. EB-PVD coatings consistently outperform APS in all categories except cost efficiency and thermal insulation, confirming their robustness and suitability for aggressive turbine environments. The integrated visual and tabular data collectively demonstrate that while APS coatings offer superior thermal insulation and cost-effectiveness, EB-PVD coatings provide better long-term durability, mechanical strength, and resistance to spallation and fatigue—making them the preferred solution for advanced turbine applications demanding extended coating lifespan and reliability.

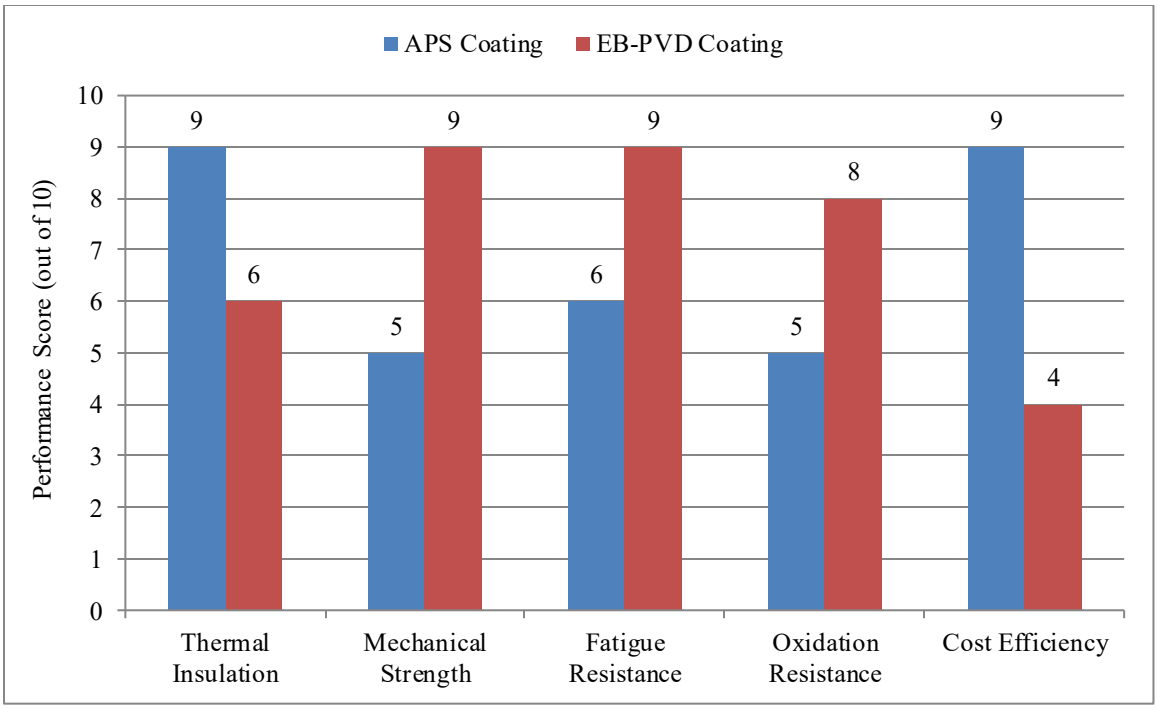

Fig. 15 Overall Summary of APS and EB-PVD Coatings

6. Discussion

The comparative analysis of Atmospheric Plasma Spray (APS) and Electron Beam Physical Vapor Deposition (EB-PVD) coatings offers new insights into the microstructural influence on Thermal Barrier Coating (TBC) performance under service-representative conditions.

6.1. Comparison with Prior Studies

The findings in this study corroborate earlier observations regarding the superior thermal insulation capabilities of APS coatings due to their porous lamellar structure [29], while also reaffirming the enhanced durability and thermal fatigue resistance of EB-PVD coatings as shown in high-temperature turbine blade applications [30]. However, unlike prior work, which primarily evaluated TBC systems in isolated thermal environments, the integration of hybrid cooling and real-time Acoustic Emission (AE) monitoring in this study enabled a more nuanced understanding of spallation onset and crack propagation dynamics. Notably, the identification of a ~300-cycle threshold for AE activity in APS systems extends earlier qualitative observations with quantitative damage progression profiles.

6.2. Implications for Turbine Applications

The implications for high-performance gas turbine operations are significant. APS coatings, despite their lower thermal conductivity (1.35 W/m·K), show rapid degradation after ~600 cycles due to non-uniform TGO growth and intersplat porosity. Conversely, EB-PVD coatings exhibit superior fatigue life, oxidation uniformity, and spallation resistance beyond 1000 cycles, underscoring their suitability for critical rotating components in harsh thermal environments. This durability, confirmed by SEM and FEA, suggests that EB-PVD coatings are better aligned with next-generation turbine requirements where operational reliability and maintenance intervals are critical constraints.

6.3. Limitations and Challenges

Despite the comprehensive methodology, several limitations must be acknowledged. First, the EB-PVD process remains cost-intensive and limited in scalability for large or complex geometries. Additionally, while FEA simulations incorporated temperature-dependent material properties, real-time material property degradation over extended thermal cycles was not dynamically modeled. The hybrid cooling system, though well-characterized, was simplified in terms of flow turbulence modeling, potentially overlooking local hot-spot effects.

6.4. Future Research Directions

Future investigations should focus on two key areas: (1) development of cost-effective, scalable EB-PVD alternatives (e.g., suspension plasma spray with columnar microstructure control), and (2) incorporation of machine learning algorithms to predict failure onset using multi-modal data (thermal imaging, AE, strain mapping). Additionally, advanced in-situ microscopy under thermal load would further elucidate microcrack nucleation mechanisms. Studies incorporating combustor gas-phase chemistry may also better reflect oxidation-induced degradation under realistic engine conditions.

7. Conclusion

This study presented a comparative evaluation of Atmospheric Plasma Spray (APS) and Electron Beam Physical Vapor Deposition (EB-PVD) Thermal Barrier Coatings (TBCs) under cyclic thermal and mechanical loads representative of turbine environments. EB-PVD coatings demonstrated significantly enhanced durability, oxidation resistance, and mechanical reliability compared to APS systems. Quantitative results showed that EB-PVD coatings maintained structural integrity beyond 1000 thermal cycles, with a Thermally Grown Oxide (TGO) thickness of 2.2–2.8 µm and peak interfacial stress around 85 MPa. In contrast, APS coatings exhibited early spallation after 580–640 cycles, with TGO thickness reaching 4.5–5.2 µm and higher interfacial stress levels (~145 MPa). While APS coatings offered superior thermal insulation—evidenced by a steeper temperature gradient of ~220°C/mm and lower thermal conductivity (1.35 ± 0.08 W/m·K)—they were more susceptible to fatigue-induced delamination and erosion. These findings suggest that EB-PVD is better suited for rotating components in aerospace and power turbines requiring high thermal fatigue resistance, whereas APS remains advantageous for stationary applications where cost and insulation performance are prioritized. Limitations include the higher cost, vacuum requirements, and line-of-sight constraints of EB-PVD, which may hinder scalability. Future work should explore nano-engineered or graded coatings, AI-driven failure prediction models, and embedded sensor-based monitoring to optimize coating lifespan and performance.

Funding Statement

This research was not supported by any specific grant from funding agencies in the public, commercial, or not-for-profit sectors. All experimental activities and computational simulations were carried out independently as part of academic research under the affiliation of Maharishi University of Information Technology.

Acknowledgments

The authors would like to express their sincere gratitude to the Department of Mechanical Engineering at Maharishi University of Information Technology for providing laboratory access and technical support throughout this study. Special thanks are extended to the National Aerospace Laboratories (NAL), Bengaluru, for facilitating the EB-PVD coating process and characterization tools. The authors also acknowledge that MD Shahbaz Ahmed and Dr. Rajiv Kumar Upadhyay contributed equally to this manuscript's conception, analysis, and preparation.

References

[1] Simone Pedrazzi, Giulio Allesina, and Paolo Tartarini, "Effects of Upgrading Systems on Energy Conversion Efficiency of a Gasifier-Fuel Cell-Gas Turbine Power Plant," *Energy Conversion and Management*, vol. 126, pp. 686-696, 2016. [CrossRef] [Google Scholar] [Publisher Link]

[2] M.A. King, and W.T. Scherer, "Inductive Modeling for Predicting Maximum Turbine Inlet Temperatures," *Proceedings of IEEE International Conference on Systems, Man and Cybernetics*, San Antonio, TX, USA, vol. 1, pp. 571-576, 1994. [CrossRef] [Google Scholar] [Publisher Link]

[3] K. Arabian, and L.H. Shu, "Sustainable Creativity: Overcoming the Challenge of Scale When Repurposing Wind-Turbine Blades," *Journal of Mechanical Design*, vol. 144, no. 10, pp. 1-10, 2022. [CrossRef] [Google Scholar] [Publisher Link]

[4] Xingye Guo, Dingyong He, and Jing Zhang, "Properties and Performance Evaluations of Thermal Barrier Coatings," *Thermal Barrier Coatings*, pp. 267-292, 2023. [CrossRef] [Google Scholar] [Publisher Link]

[5] D. Zhang, "Thermal Barrier Coatings Prepared by Electron Beam Physical Vapor Deposition (EB–PVD)," *Thermal Barrier Coatings*, pp. 3-24, 2011. [CrossRef] [Google Scholar] [Publisher Link]

[6] Benjamin Bernard et al., "Thermal Insulation Properties of YSZ Coatings: Suspension Plasma Spraying (SPS) versus Electron Beam Physical Vapor Deposition (EB-PVD) and Atmospheric Plasma Spraying (APS)," *Surface and Coatings Technology*, vol. 318, pp. 122-128, 2017. [CrossRef] [Google Scholar] [Publisher Link]

[7] Hui Peng, and Shengkai Gong, "Thermal Barrier Coatings Prepared by Electron Beam-Physical Vapor Deposition (EB-PVD)," *Thermal Barrier Coatings*, pp. 119-136, 2023. [CrossRef] [Google Scholar] [Publisher Link]

[8] Abdullah Cahit Karaoglanli, Kadir Mert Doleker, and Yasin Ozgurluk, "Interface Failure Behavior of yttria Stabilized Zirconia (YSZ), $La_2Zr_2O_7$, Gd_2Zr_2O7, YSZ/$La_2Zr_2O_7$ and YSZ/$Gd_2Zr_2O_7$ thermal Barrier Coatings (TBCs) in Thermal Cyclic Exposure," *Materials Characterization*, vol. 159, 2020. [CrossRef] [Google Scholar] [Publisher Link]

[9] Hongxu Zhao et al., "Performance Evaluation and Thermal Shock Behavior of PS-PVD $(Gd_{0.9}Yb_{0.1})_2Zr_2O_7$/YSZ Thermal Barrier Coatings," *Coatings*, vol. 12, no. 3, pp. 1-14, 2022. [CrossRef] [Google Scholar] [Publisher Link]

[10] Junxiang Gao et al., "Breakaway Oxidation Kinetics at Ceramic-Metal Interfaces: A Bidirectional Diffusion-Reaction Framework for Double-Layered Thermally Grown Oxides," *Composite Structures*, vol. 371, 2025. [CrossRef] [Google Scholar] [Publisher Link]

[11] H.Y. Chen et al., "Friction Delamination Mechanism of EB-PVD Thermal Barrier Coatings in High-Temperature and High-Speed Rotating Service Environment," *Journal of the European Ceramic Society*, vol. 43, no. 8, pp. 3637-3646, 2023. [CrossRef] [Google Scholar] [Publisher Link]

[12] Dipak K. Das et al., "Microstructure, Texture and Thermal Cycling Performance of EB-PVD TBCs Deposited under Different Processing Conditions," *High Temperature Materials and Processes*, vol. 30, no. 6, pp. 539-548, 2011. [CrossRef] [Google Scholar] [Publisher Link]

[13] Lei Zhao, Lianyong Xu, and Kamran Nikbin, "Predicting Failure Modes in Creep and Creep-Fatigue Crack Growth using a Random Grain/Grain Boundary Idealised Microstructure Meshing System," *Materials Science and Engineering: A*, vol. 704, pp. 274-286, 2017. [CrossRef] [Google Scholar] [Publisher Link]

[14] Jishen Jiang et al., "FE Analysis of the Effects of TGO Thickness and Interface Asperity on the Cracking Behavior Between the TGO and the Bond Coat," *ASME Turbo Expo 2016: Turbomachinery Technical Conference and Exposition*, Seoul, South Korea, pp. 1-10, 2016. [CrossRef] [Google Scholar] [Publisher Link]

[15] K. Rajeswari et al., "Micro Structural Control of Stabilized Zirconia Ceramics (8YSZ) through Modified Conventional Sintering Methodologies," *Science of Sintering*, vol. 42, no. 1, pp. 91-97, 2010. [CrossRef] [Google Scholar] [Publisher Link]

[16] Chengcheng Zhang et al., "Improved Parallelism of Graded W–Cu–SiC Materials by Adjusting the Coefficient of thermal Expansion," *Ceramics International*, vol. 46, no. 7, pp. 9714-9721, 2020. [CrossRef] [Google Scholar] [Publisher Link]

[17] H. Stopp, J. Grunewald, and P. Häupl, *Influence of Moisture and Air Movement in Porous Materials on Thermal Insulation*, Thermal Conductivity 23, 1st ed., CRC Press, pp.1-12, 1996. [Google Scholar] [Publisher Link]

[18] Younggil Song, and Tae Wook Heo, "Mesoscale Modeling and Semi-Analytical Approach for the Microstructure-Aware Effective Thermal Conductivity of Porous Polygranular Materials," *Computational Materials Science*, vol. 235, pp. 1-40, 2024. [CrossRef] [Google Scholar] [Publisher Link]

[19] Laura-Cebrian Ortiz, and Sumanta Acharya, "Enhancements to Impingement Heat Transfer through Nozzle Geometry Modifications," *ASME Turbo Expo 2023: Turbomachinery Technical Conference and Exposition: Heat Transfer — General Interest/Additive Manufacturing Impacts on Heat Transfer; Internal Air Systems; Internal Cooling*, Boston, Massachusetts, USA, vol. 7B, 2023. [CrossRef] [Google Scholar] [Publisher Link]

[20] Shanyou Wang, Xueying Li, and Jing Ren, "Conjugate Heat Transfer and Thermal Stress in an Impingement Cooling Unit for Gas Turbine Vane," *ASME Turbo Expo 2023: Turbomachinery Technical Conference and Exposition: Heat Transfer — General Interest/Additive Manufacturing Impacts on Heat Transfer; Internal Air Systems; Internal Cooling*, Boston, Massachusetts, USA, vol. 7B, 2023. [CrossRef] [Google Scholar] [Publisher Link]

[21] Yuyang Liu, Yu Rao, and Li Yang, "Numerical Simulations of a Double-wall Cooling with Internal Jet Impingement and External Hexagonal Arrangement of Film Cooling Holes," *International Journal of Thermal Sciences*, vol. 153, 2020. [CrossRef] [Google Scholar] [Publisher Link]

[22] Da Qiao et al., "Comprehensive Understanding of the Effect of TGO Growth Modes on Thermal Barrier Coating Failure Based on a Simulation," *Materials*, vol. 17, no. 1, pp. 1-19, 2023. [CrossRef] [Google Scholar] [Publisher Link]

[23] Matt Carter et al., "Thermomechanical Stress and Creep-Fatigue Analysis of a High-Temperature Prototype Receiver for Heating Particles," *ASME 2023 17th International Conference on Energy Sustainability collocated with the ASME 2023 Heat Transfer Summer Conference*, Washington, DC, USA, 2023. [CrossRef] [Google Scholar] [Publisher Link]

[24] Pradeep Lall, and Padmanava Choudhury, "Evolution of Fatigue Reliability of UF-Substrate Interfaces under High Temperature Exposure," *2022 21st IEEE Intersociety Conference on Thermal and Thermomechanical Phenomena in Electronic Systems (iTherm)*, San Diego, CA, USA, pp. 1-8, 2022. [CrossRef] [Google Scholar] [Publisher Link]

[25] F. Timischl, and N. Inoue, "Increasing Compositional Backscattered Electron Contrast in Scanning Electron Microscopy," *Ultramicroscopy*, vol. 186, pp. 82-93, 2018. [CrossRef] [Google Scholar] [Publisher Link]

[26] Eva Gregorová, Lucie Kotrbová, and Willi Pabst, "Thermal Cycling Damage of Silica Refractories for High-Temperature Thermal Energy Storage (HT-TES) – Can it be Healed?," *Open Ceramics*, vol. 19, pp. 1-6, 2024. [CrossRef] [Google Scholar] [Publisher Link]

[27] G. Boissonnet et al., "Phase Stability and Thermal Insulation of YSZ and Erbia-yttria Co-doped Zirconia EB-PVD Thermal Barrier Coating Systems," *Surface and Coatings Technology*, vol. 389, pp. 1-19, 2020. [CrossRef] [Google Scholar] [Publisher Link]

[28] K. Mital Subodh et al., "Modeling of the Influence of a Damaged Thermally Grown Oxide (TGO) Layer in an Environmental Barrier Coating System," *American Society of Composites (ASC) 34th Technical Conference*, Atlanta, GA, pp. 1-27, 2019. [CrossRef] [Google Scholar] [Publisher Link]

[29] Jianan Song et al., "Effect of Non-Uniform Growth of TGO Layer on Cracking Behaviors in Thermal Barrier Coatings: A Numerical Study," *Surface and Coatings Technology*, vol. 370, pp. 113-124, 2019. [CrossRef] [Google Scholar] [Publisher Link]

[30] Chen Deng et al., "Construction of Three-Dimensional Dynamic Growth TGO (Thermally Grown Oxide) Model and Stress Simulation of 8YSZ Thermal Barrier Coating," *Ceramics International*, vol. 48, no. 4, pp. 5327-5337, 2022. [CrossRef] [Google Scholar] [Publisher Link]